DOI: 10.13009/EUCASS2023-657
Aerospace Europe Conference 2023 – 10TH EUCASS – 9TH CEAS

Simplified Numerical Modeling of Film Cooling and Mixture Ratio Bias in Liquid Rocket Thrust Chambers

G. Cocirla[⋆†], *M. Grossi*[⋆], *M.T. Migliorino*[⋆], *D. Bianchi*[⋆], *F. Nasuti*[⋆]
[⋆] *Dept. of Mechanical and Aerospace Engineering - Sapienza University of Rome*
Via Eudossiana 18, 00184 - Rome, Italy
gianluca.cocirla@uniroma1.it · marco.grossi@uniroma1.it · mariotindaro.migliorino@uniroma1.it
daniele.bianchi@uniroma1.it · francesco.nasuti@uniroma1.it
[†]Corresponding author

Abstract
High performance liquid rocket engines are characterized by high pressure and high wall heat fluxes which have to be inevitably managed by an active cooling system. The most commonly used is the regenerative cooling system, which, however, may result insufficient. In such cases, cooling capabilities can be enhanced by other active cooling means, like film cooling or mixture ratio bias of peripheral injectors. The additional active cooling system has a cost in terms of performance. The present numerical parametric study provides a general cost-benefit analysis of this cooling systems in an oxygen-methane engine.

1. Introduction

Liquid rocket engine (LRE) operations may be characterized by heat fluxes released by combustion and chemical reactions greater than 100 MW/m^2. This high amount of heat can be responsible for a wall temperature exceeding the maximum admissible one for wall material integrity, which is around 850 K for metallic materials used in thrust chambers.[1] Therefore, heat transfer analysis is of paramount importance throughout the design, testing, and failure investigations of LREs.
As a trade-off between overall engine efficiency and safe structural life, active cooling systems are needed to suitably extract heat from the hot-gas flow and maintain a reasonably low temperature in order to avoid thermal failure of the wall material.[2] Nevertheless, a regenerative cooling system alone is insufficient in high-performance rocket engines because of pressure drops in cooling channels as well as manufacturing and structural limits. For such reasons, regenerative cooling system requirements can be relieved with additional active cooling techniques.
Film cooling is a method used for insulating the combustion chamber and nozzle walls against high thermal loads. A controlled flow of coolant is introduced either in liquid or gaseous phase as a thin film through annular slots or discrete holes, for example placed at the outer row of the injection plate[3] or in the nozzle.[4] The mass flow rate typically used for this purpose is in the range between 1 and 6% of the total mass flow rate, yielding a performance loss.
Mixture ratio bias, or zoned combustion, is another possible thrust chamber cooling strategy. The local mixture ratio of the outer peripheral propellant injectors is changed with respect to the core injectors, typically achieving fuel-rich conditions. This yields a reduced convective wall heat flux thanks to the lower temperature combustion products.
Film cooling and mixture ratio bias might represent an interesting choice, especially when in combination with other cooling techniques such as regenerative cooling, achieving high performances and protecting those engines which operate at significantly high pressure, and thus undergo significantly high thermal loads. In this framework, computational fluid dynamic (CFD) simulations play a fundamental role because of their versatility and capability to save resources with respect to more expensive procedures such as hot-firing tests.
In the present study, a simplified numerical modeling of film cooling and mixture ratio bias in liquid rocket thrust chambers is presented. The computational approach is based on axisymmetric Reynolds-averaged Navier-Stokes (RANS) simulations, with sub-models accounting for the effects of turbulence, chemistry, and radiation.[5] CFD simulations are employed to perform an extensive parametric analysis for investigating the effects of the driving parameters on wall heat flux and engine performance. Film cooling parameters include film injection mass flow rate, slot height, temperature, and blowing ratio. For the zoned combustion analysis the parameters investigated are the bias mass flow rate and mixture ratio. The reference chamber geometry and operating conditions are inspired from the seven-injector thrust chamber burning gaseous oxygen and gaseous methane of the technical university of Munich (TUM).[6–8]

DOI: 10.13009/EUCASS2023-657

Film cooling and mixture ratio bias are investigated in terms of their beneficial effect on the wall heat flux reduction, but also on the resulting loss in specific impulse. Different reaction mechanisms with increasing fidelity are also considered and compared.

2. Numerical Model

The numerical study is carried out using an in-house three-dimensional finite-volume RANS solver, capable to handle multi-component mixtures of turbulent, reactive, compressible, and thermally perfect gases.[9–13] The compressible RANS equations for reacting mixtures[14] are solved:

$$\begin{aligned} &\frac{\partial(\rho y_i)}{\partial t} + \nabla\cdot(\rho \mathbf{v} y_i) = -\nabla\cdot\mathbf{j}_i + \dot{\omega}_i \qquad (i = 1, ..., N_\mathrm{s}) \\ &\frac{\partial(\rho \mathbf{v})}{\partial t} + \nabla\cdot(\rho\mathbf{v}\mathbf{v}) = \nabla\cdot\mathbf{S} \\ &\frac{\partial(\rho e_0)}{\partial t} + \nabla\cdot(\rho\mathbf{v}e_0) = \nabla\cdot(\mathbf{v}\cdot\mathbf{S}) - \nabla\cdot\mathbf{q} \end{aligned} \tag{1}$$

where the mixture total energy per unit mass e_0 is defined as:

$$e_0 = \sum_{i=1}^{N_\mathrm{s}} y_i(e_i + \Delta e^\circ_{\mathrm{f},i}) + \frac{\mathbf{v}\cdot\mathbf{v}}{2} \tag{2}$$

The quantities under divergence sign on the right hand side of Eq.(1), defined in Eq.(3), respectively represent the mass diffusion flux vector of the i-th species, the stress tensor, and the heat flux vector.

$$\begin{aligned} \mathbf{j}_i &= -\left(\frac{\mu}{\mathrm{Sc}} + \frac{\mu_\mathrm{T}}{\mathrm{Sc}_\mathrm{T}}\right)\nabla y_i \\ \mathbf{S} &= -p\mathbf{I} - (\mu + \mu_\mathrm{T})\left\{\frac{2}{3}(\nabla\cdot\mathbf{v})\mathbf{I} + \left[\nabla\mathbf{v} + (\nabla\mathbf{v})^\mathrm{T}\right]\right\} \\ \mathbf{q} &= -\left(k + \frac{\mu_\mathrm{T}}{\mathrm{Pr}_\mathrm{T}}\sum_{i=1}^{N_\mathrm{s}} y_i c_{p,i}\right)\nabla T + \sum_{i=1}^{N_\mathrm{s}}\left(h_i + \Delta h^\circ_{\mathrm{f},i}\right)\mathbf{j}_i \end{aligned} \tag{3}$$

Note that the mass fluxes $\mathbf{j_i}$ are corrected to ensure that they sum to zero by distributing the residual according to the species mass fraction.[15] This correction allows to obtain results close to formulations based on gradients of molar mass fractions (Hirschfelder approximation[16]). Thermodynamic closure is obtained assuming a thermally perfect gas mixture, governed by the equation of state:

$$p = \rho R T \quad \text{with} \quad R = \sum_{i=1}^{N_\mathrm{s}} y_i R_i \tag{4}$$

where R_i is the species gas constant. The caloric equation of state is obtained expressing constant pressure specific heats as a function of temperature according to the seventh-order polynomial written for each species:

$$\begin{aligned} c_{p,i}(T) = &a_{1,i}T^{-2} + a_{2,i}T^{-1} + a_{3,i} + a_{4,i}T + \\ &+ a_{5,i}T^2 + a_{6,i}T^3 + a_{7,i}T^4 \qquad (i = 1, ..., N_\mathrm{s}) \end{aligned} \tag{5}$$

with coefficients $a_{1,i}, a_{2,i}, \ldots, a_{7,i}$ reported in Ref.[17] The standard heat of formation for the i-th species $\Delta h^\circ_{\mathrm{f},i}$ is also taken from Ref.[17] The molecular transport properties μ and k are derived from those of the individual species according to Wilke's rule,[14] and those of individual species are taken from the fourth-order polynomials of temperature reported in Ref.[18] Species diffusion is considered to be the same for all the N_s species through a constant Schmidt number, assumed as Sc = 0.7. Turbulent viscosity μ_T is evaluated by the integration of an additional convection/diffusion equation, according to the Spalart-Allmaras one-equation model,[19] whose standard constants are used for model closure. Turbulent diffusivity and conductivity are evaluated on the basis of μ_T through constant turbulent Schmidt and Prandtl numbers, $\mathrm{Sc}_T = 0.7$ and $Pr_\mathrm{T} = 0.9$, respectively.
The chemical source terms $\dot{\omega}_i$ in Eqs. (1) are obtained by the contribution of each of the N_r reactions as:

DOI: 10.13009/EUCASS2023-657

$$\dot{\omega}_i = \mathcal{M}_i \sum_{j=1}^{N_r} (\nu^{P}_{i,j} - \nu^{R}_{i,j}) \left[k_{f,j} \prod_{s=1}^{N_s} \left(\frac{\rho_s}{\mathcal{M}_s} \right)^{\nu^{R}_{s,j}} - k_{b,j} \prod_{s=1}^{N_s} \left(\frac{\rho_s}{\mathcal{M}_s} \right)^{\nu^{P}_{s,j}} \right] \alpha_j \tag{6}$$

where the generic reaction among species B_i is expressed with stoichiometric coefficients of reactants $\nu^{R}_{i_j}$ and products $\nu^{P}_{i_j}$ as:

$$\sum_{i=1}^{N_s} \nu^{R}_{i,j} B_i \rightleftharpoons \sum_{i=1}^{N_s} \nu^{P}_{i,j} B_i \qquad (j = 1, ..., N_r) \tag{7}$$

with forward $k_{f,j}$ and backward $k_{b,j}$ reaction rates expressed as:

$$k_{f,j} = A_j\, T^{n_j} \exp\left(-\frac{E_{a,j}}{\mathcal{R}T} \right) \qquad k_{b,j} = k_{f,j}/K_j \tag{8}$$

where A_j is the pre-exponential factor, n_j the temperature exponent, $E_{a,j}$ the molar activation energy, $\mathcal{R}$ the universal gas constant, and K_j the equilibrium constant of the j-th reaction evaluated from thermodynamic data taken from Ref.[17] The coefficient α_j is generally equal to one, except for the case of reactions involving a generic third body M; in such a case, it is defined as:

$$\alpha_j = \sum_{i=1}^{N_s} \hat{\alpha}_{i,j} \left(\frac{\rho_i}{\mathcal{M}_i} \right) \tag{9}$$

where $\hat{\alpha}_{i,j}$ is the third-body efficiency of the i-th species when involved in the j-th reaction.
Finite-rate chemistry plays an essential role in the flowfield simulation and consequently in the performance and wall heat flux estimation. In order to ensure the quality of the results, two reaction mechanisms of increasing reliability and complexity are used and compared in the present study. The first one is the modified Jones-Lindstedt global reaction mechanism for oxygen/methane mixtures, referred hereafter as JLR and reported in Table 1. JLR has been introduced and validated in the range 10-100 bar in Ref.[11] This mechanism includes three additional species and three extra reactions with respect to the original one[20,21] with the goal of taking into account recombination reactions of dissociated species.

Table 1: JLR global reaction mechanism for oxygen/methane mixtures.[11]

j	Reaction	A_j	n_j	$E_{a,j}/\mathcal{R}$
1	$\frac{1}{2}CH_4 + \frac{5}{4}O_2 \longrightarrow CO + 2H_2 + \frac{3}{4}O_2 - \frac{1}{2}CH_4$	$4.40 \cdot 10^{11}$	0.00	15096.6
2	$CH_4 + H_2O \longrightarrow CO + 3H_2$	$3.00 \cdot 10^{08}$	0.00	15096.6
3	$CO + H_2O \rightleftharpoons CO_2 + H_2$	$2.75 \cdot 10^{09}$	0.00	10064.4
4	$\frac{1}{4}H_2 + \frac{3}{2}O_2 \rightleftharpoons H_2O + O_2 - \frac{3}{4}H_2$	$6.80 \cdot 10^{15}$	-1.00	20128.8
5	$O_2 \rightleftharpoons 2O$	$1.50 \cdot 10^{09}$	0.00	56863.8
6	$H_2O \rightleftharpoons H + OH$	$2.30 \cdot 10^{22}$	-3.00	60386.3
7	$OH + H_2 \rightleftharpoons H + H_2O$	$2.10 \cdot 10^{05}$	1.51	1726.0

Units are expressed in kmoles, meters, seconds, and Kelvin.

The JLR global mechanism is compared with the skeletal mechanism TSR-CDF-13, proposed in Ref.[22] and reported in Table 2. The TSR-CDF-13 is the result of a reduction of the detailed chemical kinetics mechanism for oxygen/methane mixtures at high pressures developed by Zhukov[23] employing an algorithm based on the computational singular perturbation theory. It should be noted that the reduction strategy presented in Ref.[22] gave birth to a family of skeletal reaction mechanisms, with different number of species and reactions and, thus, with different accuracy. The TSR-CDF-13 reaction mechanism has been specifically developed to deal with the CFD analysis of rocket engines thrust chambers. The decision to choose the TSR-CDF-13 mechanism, which is neither the most accurate nor the least, relies on the reasonable compromise between the accuracy it showed during validation and computational cost. Therefore, the selected skeletal reaction mechanism retains the species already included in the JLR global mechanism, with the addition of further four, namely HO_2, CH_3, HCO, and CH_2O, for a total of 13 species and 46 reactions. The reaction set includes 10 three-body reactions, with efficiencies reported in Table 3, and 3 fall-off reactions. Fall-off reactions rely on two sets of Arrhenius coefficients, and thus on two preliminary reaction rates k_{f0} and k_∞, for the determination of the actual reaction rate k_f.[24,25]

DOI: 10.13009/EUCASS2023-657

Table 2: TSR-CDF-13 reduced skeletal reaction mechanism for oxygen/methane mixtures.[22]

j	Reaction	A_j	n_j	$E_{a,j}/\mathcal{R}$ (K)
1	$2O + M \rightleftharpoons O_2 + M$	$1.20 \cdot 10^{14}$	-1.00	0.0
2	$H + O + M \rightleftharpoons OH + M$	$5.00 \cdot 10^{14}$	-1.00	0.0
3	$H_2 + O \rightleftharpoons H + OH$	$5.00 \cdot 10^{01}$	2.67	3165.2
4	$HO_2 + O \rightleftharpoons O_2 + OH$	$2.00 \cdot 10^{10}$	0.00	0.0
5	$CH_3 + O \rightleftharpoons CH_2O + H$	$8.43 \cdot 10^{10}$	0.00	0.0
6	$CH_4 + O \rightleftharpoons CH_3 + OH$	$1.02 \cdot 10^{06}$	1.50	4327.7
7	$CO + O + M \rightleftharpoons CO_2 + M$	$6.02 \cdot 10^{11}$	0.00	1509.7
8	$HCO + O \rightleftharpoons CO + OH$	$3.00 \cdot 10^{10}$	0.00	0.0
9	$HCO + O \rightleftharpoons CO_2 + H$	$3.00 \cdot 10^{10}$	0.00	0.0
10	$CH_2O + O \rightleftharpoons HCO + OH$	$3.90 \cdot 10^{10}$	0.00	1781.4
11	$CO + O_2 \rightleftharpoons CO_2 + O$	$2.50 \cdot 10^{09}$	0.00	24053.9
12	$CH_2O + O_2 \rightleftharpoons HCO + HO_2$	$1.00 \cdot 10^{11}$	0.00	20128.8
13	$H + O_2 + M \rightleftharpoons HO_2 + M$	$2.80 \cdot 10^{15}$	-0.86	0.0
14	$H + 2O_2 \rightleftharpoons HO_2 + O_2$	$3.00 \cdot 10^{14}$	-1.72	0.0
15	$H + H_2O + O_2 \rightleftharpoons H_2O + HO_2$	$9.38 \cdot 10^{12}$	-0.76	0.0
16	$H + O_2 \rightleftharpoons O + OH$	$8.30 \cdot 10^{10}$	0.00	7252.9
17	$2H + M \rightleftharpoons H_2 + M$	$1.00 \cdot 10^{15}$	-1.00	0.0
18	$2H + H_2 \rightleftharpoons 2H_2$	$9.00 \cdot 10^{10}$	-0.60	0.0
19	$2H + H_2O \rightleftharpoons H_2 + H_2O$	$6.00 \cdot 10^{13}$	-1.25	0.0
20	$CO_2 + 2H \rightleftharpoons CO_2 + H_2$	$5.50 \cdot 10^{14}$	-2.00	0.0
21	$H + OH + M \rightleftharpoons H_2O + M$	$2.20 \cdot 10^{19}$	-2.00	0.0
22	$H + HO_2 \rightleftharpoons H_2O + O$	$3.97 \cdot 10^{09}$	0.00	337.7
23	$H + HO_2 \rightleftharpoons H_2 + O_2$	$2.80 \cdot 10^{10}$	0.00	537.4
24	$H + HO_2 \rightleftharpoons 2OH$	$1.34 \cdot 10^{11}$	0.00	319.5
25[a]	$CH_3 + H(+M) \rightleftharpoons CH_4(+M)$	$1.27 \cdot 10^{13}$	-0.63	192.7
		$2.48 \cdot 10^{30}$	-4.76	1227.9
26	$CH_4 + H \rightleftharpoons CH_3 + H_2$	$6.60 \cdot 10^{05}$	1.62	5454.9
27[a]	$H + HCO(+M) \rightleftharpoons CH_2O(+M)$	$1.09 \cdot 10^{09}$	0.48	-130.8
		$1.35 \cdot 10^{21}$	-2.57	717.1
28	$H + HCO \rightleftharpoons CO + H_2$	$7.34 \cdot 10^{10}$	0.00	0.0
29	$CH_2O + H \rightleftharpoons H_2 + HCO$	$2.30 \cdot 10^{08}$	1.05	1648.0
30[a]	$CO + H_2(+M) \rightleftharpoons CH_2O(+M)$	$4.30 \cdot 10^{04}$	1.50	40056.2
		$5.07 \cdot 10^{24}$	-3.42	42446.5
31	$H_2 + OH \rightleftharpoons H + H_2O$	$2.16 \cdot 10^{05}$	1.51	1726.0
32	$2OH \rightleftharpoons H_2O + O$	$3.57 \cdot 10^{01}$	2.40	-1061.8
33	$HO_2 + OH \rightleftharpoons H_2O + O_2$	$2.90 \cdot 10^{10}$	0.00	-251.6
34	$CH_4 + OH \rightleftharpoons CH_3 + H_2O$	$1.00 \cdot 10^{05}$	1.60	1570.0
35	$CO + OH \rightleftharpoons CO_2 + H$	$4.75 \cdot 10^{04}$	1.23	35.2
36	$HCO + OH \rightleftharpoons CO + H_2O$	$5.00 \cdot 10^{10}$	0.00	0.0
37	$CH_2O + OH \rightleftharpoons H_2O + HCO$	$3.43 \cdot 10^{06}$	1.18	-224.9
38	$CH_3 + HO_2 \rightleftharpoons CH_4 + O_2$	$1.00 \cdot 10^{09}$	0.00	0.0
39	$CO + HO_2 \rightleftharpoons CO_2 + OH$	$1.50 \cdot 10^{11}$	0.00	11876.0
40	$CH_3 + O_2 \rightleftharpoons CH_2O + OH$	$3.60 \cdot 10^{07}$	0.00	4498.8
41	$CH_3 + HCO \rightleftharpoons CH_4 + CO$	$2.65 \cdot 10^{10}$	0.00	0.0
42	$CH_2O + CH_3 \rightleftharpoons CH_4 + HCO$	$3.32 \cdot 10^{00}$	2.81	2948.9
43	$H_2O + HCO \rightleftharpoons CO + H + H_2O$	$2.24 \cdot 10^{15}$	-1.00	8554.7
44	$HCO + M \rightleftharpoons CO + H + M$	$1.87 \cdot 10^{17}$	-1.00	8554.7
45	$HCO + O_2 \rightleftharpoons CO + HO_2$	$7.60 \cdot 10^{09}$	0.00	201.3
46	$CH_3 + OH \rightleftharpoons CH_2O + H_2$	$8.00 \cdot 10^{09}$	0.00	0.0

Units are expressed in kmoles, meters, seconds, and Kelvin.

[a]Fall-off reaction. k_{f0} and k_∞ Arrhenius coefficients are reported in the first and second row, respectively.

DOI: 10.13009/EUCASS2023-657

Table 3: Third-body efficiencies associated to the TSR-CDF-13 reduced skeletal reaction mechanism.[22]

j	Reaction	$\hat{\alpha}_{CH_4}$	$\hat{\alpha}_{CO}$	$\hat{\alpha}_{CO_2}$	$\hat{\alpha}_{H_2}$	$\hat{\alpha}_{H_2O}$	$\hat{\alpha}_{O_2}$
1	$2\,O + M \rightleftarrows O_2 + M$	2.00	1.75	3.60	2.40	15.40	1.00
2	$H + O + M \rightleftarrows OH + M$	2.00	1.50	2.00	2.00	6.00	1.00
7	$CO + O + M \rightleftarrows CO_2 + M$	2.00	1.50	3.50	2.00	6.00	6.00
13	$H + O_2 + M \rightleftarrows HO_2 + M$	1.00	0.75	1.50	1.00	0.00	0.00
17	$2\,H + M \rightleftarrows H_2 + M$	2.00	1.00	0.00	0.00	0.00	1.00
21	$H + OH + M \rightleftarrows H_2O + M$	2.00	1.00	1.00	0.73	3.65	1.00
25	$CH_3 + H + M \rightleftarrows CH_4 + M$	2.00	1.50	2.00	2.00	6.00	1.00
27	$H + HCO + M \rightleftarrows CH_2O + M$	2.00	1.50	2.00	2.00	6.00	1.00
30	$CO + H_2 + M \rightleftarrows CH_2O + M$	2.00	1.50	2.00	2.00	6.00	1.00
44	$HCO + M \rightleftarrows CO + H + M$	2.00	1.50	2.00	2.00	0.00	1.00

The governing equations (Eq.(1)) are numerically integrated up to the wall. The solver adopts a finite volume Godunov-type formulation. To allow a second-order accuracy in space, a linear cell reconstruction of flow variables is carried out by using the value in the considered cell and those in the contiguous ones. A Roe approximate Riemann solver[26] for multi-block structured meshes is used. This allows to evaluate variables at cell interfaces and associated fluxes to compute the evolution in time. Time integration adopts the Strang operator-splitting technique:[27] convective and diffusive terms are integrated by a second-order Runge-Kutta scheme, whereas for the chemical source terms a stiff ordinary differential equation implicit integrator is used.[28]

3. Test Case and Computational Setup

The selected test case for the present study is a seven-injector thrust chamber burning gaseous oxygen and gaseous methane.[6–8] The thrust chamber is composed of five water-cooled segments. The total length of the four combustion chamber segments and the nozzle one is 383 mm. The combustion chamber diameter is 30 mm and the throat diameter is 19 mm, resulting in a contraction ratio of 2.5. The reference operating mean combustion chamber pressure is 18.3 bar, the mixture ratio is 2.65, and the total mass flow rate is 0.291 kg/s. Table 4 summaries the main thrust chamber dimensions and the operating conditions.

Table 4: Summary of seven-injector TUM thrust chamber dimensions and operating conditions.[8]

Chamber diameter	d_c	30.0 mm
Throat diameter	d_t	19.0 mm
Total thrust chamber length	x_{tot}	382.0 mm
Axial loxation end of segment A	x_A	145.0 mm
Axial loxation end of segment B	x_B	222.0 mm
Axial loxation end of segment C	x_C	299.0 mm
Axial loxation end of segment D	x_D	340.0 mm
Combustion chamber pressure	p_c	18.3 bar
Total mixture ratio	O/F_{tot}	2.65
Total mass flow rate	$\dot{m}_{tot}$	0.291 kg/s
Oxidizer mass flow rate	$\dot{m}_o$	0.211 kg/s
Fuel mass flow rate	$\dot{m}_f$	0.080 kg/s

The already validated[12] simplified CFD approach is adopted to carry out the parametric analysis. In Ref.[12] combustion products at chemical equilibrium were injected in the combustion chamber through the whole injection plate area. In this study a modification is introduced to such an approach, maintaining at the same time its characteristic simplicity and low computational burden. In particular, a backward-facing step of 3 mm is introduced at the injection plate between the hot gas inflow and the upper wall (see Fig. 1a), yielding a more realistic injection geometry. Film cooling and mixture ratio bias configurations are devised as a further modification of the geometry as illustrated in Figs. 1b and 1c. The configuration without film cooling or mixture ratio bias (Fig. 1a) is assumed to be the reference case to which the obtained results are compared.

DOI: 10.13009/EUCASS2023-657

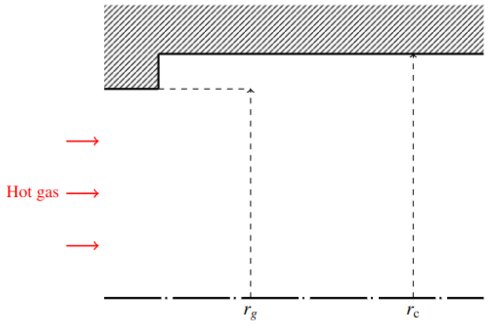

(a) Scheme of the reference simulation.

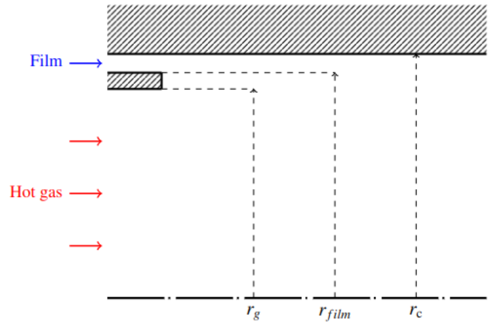

(b) Scheme of film cooling simulation.

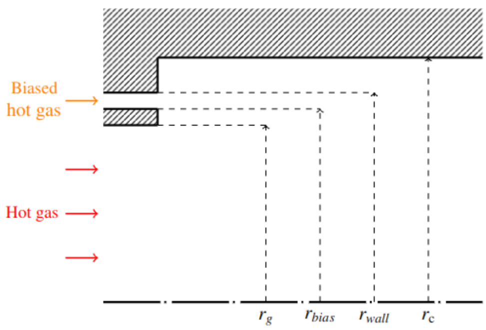

(c) Scheme of mixture ratio bias simulation.

Figure 1: Schemes of near-injector region. Not to scale.

On the left hand side of the setup, subsonic inflow conditions are applied, and adiabatic no-slip conditions are imposed to the vertical walls. Mass flow rate, total temperature, and mixture composition in terms of the species included in the chemical reaction mechanism are prescribed at the inflow boundaries. It is worth to point out that in the film cooling configurations a pure gaseous methane is assumed as the film coolant, while, in the mixture ratio bias cases, peripheral cold mixture is possibly composed of all the species involved in the chemical reaction mechanism, depending on the local O/F value. The CEA program[18] is used to compute total temperature and equilibrium mass fractions at the design chamber pressure and mixture ratio assuming reactants in gaseous phase. Symmetry is enforced at the centerline. The upper wall is characterized by a no-slip, non-catalytic, and isothermal boundary condition. For the sake of simplicity, a wall temperature of 400 K, similar to that of the thrust chambers described in Refs.,[6,12] has been selected. The outflow is supersonic.

The computational grid is a single-block 2-D axisymmetric 100×100 structured grid for both film cooling and mixture ratio bias simulations. The near-injector region is shown in Fig. 2. A cell clustering toward the upper wall is used over the whole chamber length to properly resolve the viscous sublayer, resulting in a non-dimensional wall distance $y^+ \simeq 1$. On the other hand, in the axial direction, the domain is divided into three zones to reasonably resolve the main features of the flowfield, namely an injection, streamtube, and nozzle region. Furthermore, as shown in Fig. 2, a proper cell clustering is also introduced in the radial direction to sufficiently resolve the mixing layer and the recirculation region between the hot gas and cold fluid inflows. A uniform streamtube region is identified from the end of the injection zone until the nozzle entrance. Eventually, the nozzle region extends until the end of the thrust chamber. Cells are here clustered toward the throat to properly resolve the subsonic to supersonic transition and to manage the higher axial gradients. Smooth transitions between mesh regions are guaranteed by a suitable axial cell clustering, which allows to consider larger cells where the propellants are mixed and hence to reduce computational time. Note that the computational domain shown in Fig. 2 is referred to a particular configuration. Minimal variations in the discretization of the near-injector region are made in the parametric analysis, when the cold fluid slot injection height is changed, while the cell number and the grid topology are fixed.

DOI: 10.13009/EUCASS2023-657

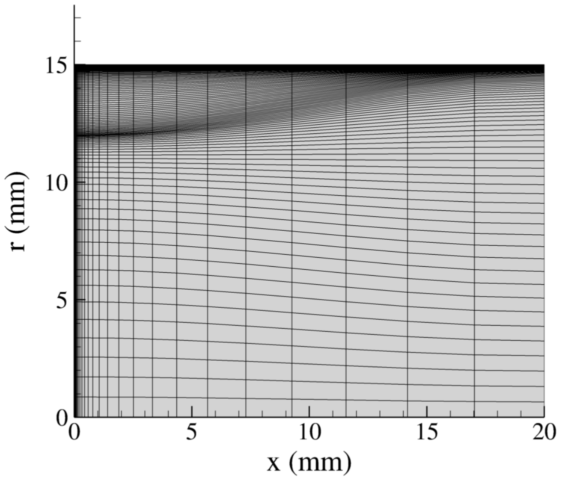

Figure 2: Near-injector region computational grid.

4. Film Cooling Analysis

In this section, a parametric analysis is performed aiming at evaluating the cylinder and throat wall heat fluxes reduction and performance loss in terms of the four identified driving parameters, namely, the film mass flow rate ratio ($\dot{m}_{film}/\dot{m}_{tot}$), the film injection slot height ($w_{slot} = r_c - r_{film}$), the film injection temperature (T_{film}), and the blowing ratio ($B = \rho u_f/\rho u_g$). Numerical correlations are provided as a function of the observed most relevant quantities as efficient and versatile numerical tools for film-cooled LRE design. The role of finite rate chemical kinetics is also investigated, comparing obtained fields, wall heat fluxes, and performance with two reaction mechanisms (JLR and TSR-CDF-13). The simulation matrix is summarized in Table 5. If not specified, the total mass flow rate and total mixture ratio of Table 4, a film injection temperature of 500 K, a uniform wall temperature of 400 K, and the JLR global reaction mechanism are considered. Cylinder and nozzle convective wall heat fluxes and specific impulse variation with respect to the reference test case are also reported. Note that positive values represent an increase of the observed quantity, while negative ones represent a reduction.

Table 5: Summary of film cooling parametric analysis obtained varying film mass flow rate ratio and film injection slot.

TEST	$\frac{\dot{m}_{film}}{\dot{m}_{tot}}$	w_{slot} (μm)	B	O/F_{inj}	O/F_{tot}	$\frac{\Delta q_w}{q_{w,ref}}\Big\rvert_{cyl}$	$\frac{\Delta q_w}{q_{w,ref}}\Big\rvert_{noz}$	$\frac{\Delta I_{sp}}{I_{sp,ref}}$ (%)
1[a]	0	0.0	0.000	2.650	2.650	0	0	0
2[a]	0.01	100.0	0.487	2.750	2.650	-0.0255	-0.0004	0.07
3[a]	0.02	100.0	0.985	2.859	2.650	-0.0478	-0.0015	0.09
4	0.03	100.0	1.492	2.976	2.650	-0.0688	-0.0043	0.08
5	0.05	100.0	2.540	3.242	2.650	-0.1130	-0.0156	-0.03
6[a]	0.10	100.0	5.361	4.173	2.650	-0.2430	-0.0857	-0.75
7[b]	0.01	50.0	0.975	2.750	2.650	-0.0256	0	0.07
7.1	0.01	50.0	0.975	2.650	2.556	-0.0392	-0.0147	-0.15
8	0.02	50.0	1.970	2.859	2.650	-0.0480	0	0.10
8.1	0.02	50.0	1.970	2.650	2.466	-0.0750	-0.0321	-0.41
9	0.03	50.0	2.985	2.976	2.650	-0.0700	-0.0030	0.10
9.1	0.03	50.0	2.985	2.650	2,381	-0.1100	-0.0531	-0.76
10	0.05	50.0	5.080	3.242	2.650	-0.1180	-0.0147	0.05
11	0.01	25.0	1.956	2.750	2.650	-0.0253	-0.0002	0.08
12	0.02	25.0	3.951	2.859	2.650	-0.0486	-0.0006	0.10
13	0.03	25.0	5.988	2.976	2.650	-0.0723	-0.0023	0.11

[a] Both JLR and TSR-CDF-13 are employed.

[b] Different film cooling injection temperatures are considered.

DOI: 10.13009/EUCASS2023-657

4.1 Film injection temperature effect

Test 7 from Table 5 is taken into account in order to investigate the effect of the film injection temperature considering the same film mass flow rate and film injection slot height. The injection temperature is varied from 400 to 600 K. In Fig. 3 the convective wall heat flux of the selected thrust chamber is reported. It is clear from Fig. 3 that the injection temperature has a marginal effect on the wall heat transfer, and that this effect is limited only to the first few millimeters of the chamber. Also a negligible variation in terms of specific impulse is present. This is expected, as the hot gases in the core flow are at approximately 3300 K and the variation of the film injection temperature is of only 100 K around the nominal value (500 K).

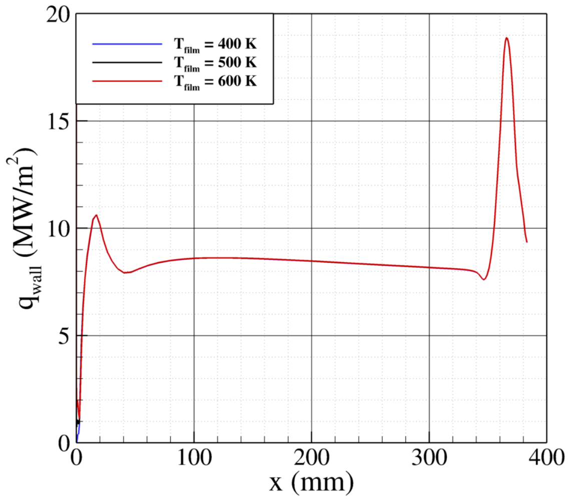

Figure 3: Film injection temperature effect on convective wall heat flux for Test 7.

4.2 Film injection slot height effect

Tests 4, 9 and 13 from Table 5 are taken into account in order to discuss the effect of the film injection slot height on the flowfield, wall heat flux, and performance. The three considered tests have the same film mass flow rate and film injection temperature. A decrease in film injection slot height w_{slot} results in an increase of film mass flux ρu_f and therefore in the blowing ratio B. The effect of a different film injection slot height or blowing ratio is important especially in the first segment of the thrust chamber (see Fig. 4), while it is relatively negligible in the nozzle region.

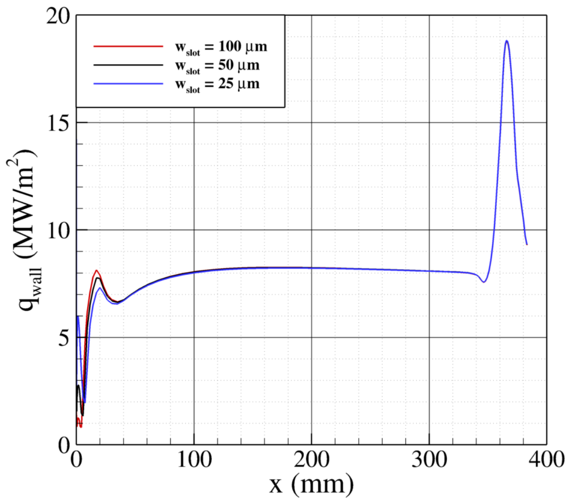

Figure 4: Film injection slot height effect on convective wall heat flux for Tests 4, 9 and 13.

DOI: 10.13009/EUCASS2023-657

It is interesting to investigate the effect of different blowing ratios on the near-injector region where the major distinctions can be observed (Fig. 5). A wide recirculation zone is observed to occur at the top-left corner of the combustion chamber. The vortex is observed to move downstream and to gradually flatten toward the upper wall as the film injection slot height is decreased, allowing the coolant to remain in the close proximity of the upper wall for a longer length, extracting less heat at the very beginning, but cooling more the wall downstream. Nevertheless, the effects of the film slot height are deemed as second order with respect to the changes in film mass flow rate.

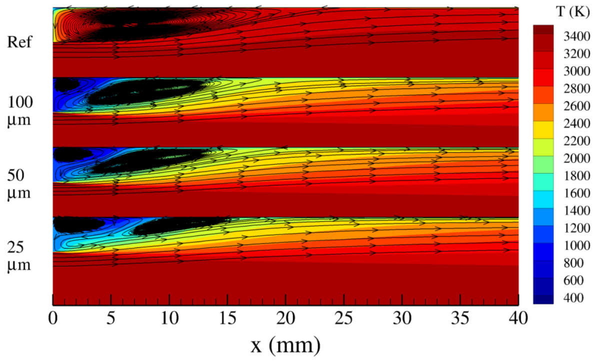

(a) Temperature contours and streamlines.

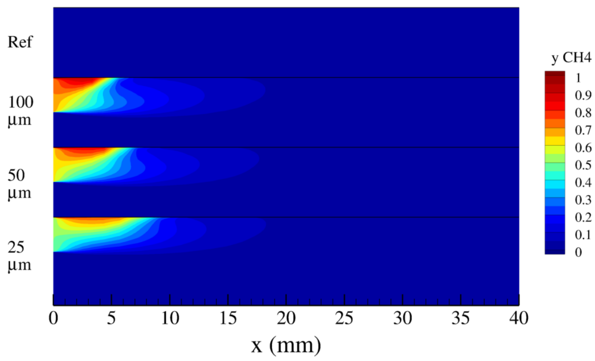

(b) Methane mass fraction.

Figure 5: Film injection slot height effect on near-injector flowfield for Tests 4, 9, and 13. Flowfields are shifted in the radial direction and zoomed in the first part of the combustion chamber for visualization purposes.

4.3 Film mass flow rate effect

Tests 2 to 6 (Table 5), characterized by the same film injection slot height and film injection temperature, are taken into account in this subsection in order to analyze the effect of the film mass flow rate ratio preserving the total mass flow rate and the total mixture ratio reported in Table 4. A fixed amount of fuel mass flow rate is distributed between the main flow and the film injection. The relevant effect of additional cooling due to an increase of film mass flow rate is shown in Fig. 6.

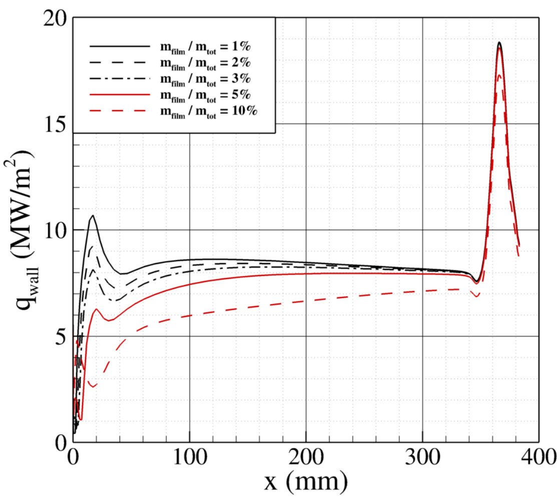

(a) Convective wall heat flux.

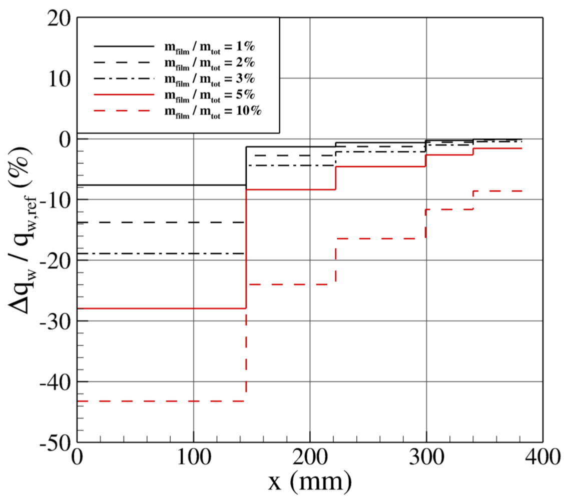

(b) Averaged convective wall heat flux.

Figure 6: Film mass flow rate effect on convective heat transfer at constant total mixture ratio for Tests 2-6.

DOI: 10.13009/EUCASS2023-657

Assuming all other parameters constant, an increase in film mass flow rate results in an increase in blowing ratio. This alters the temperature and methane mass fraction fields as shown in Fig. 7. Different blowing ratios yield different flowfield evolution with a significant impact on the near-injector region. Similarly to Fig. 5, the top-left recirculation zone moves downstream and gradually flattens toward the upper wall as the film mass flow rate is increased leading to more efficient film cooling heat extraction capacity. A visible effect is obtained on the nozzle wall heat flux for film mass flow rates above 3% of the total mass flow rate. It is interesting to notice that tests 6 and 13, which have similar blowing ratios (approximately 5.4 and 6, respectively), show much different flowfield features, due to the changes in O/F and mass flow rate of the core flow.

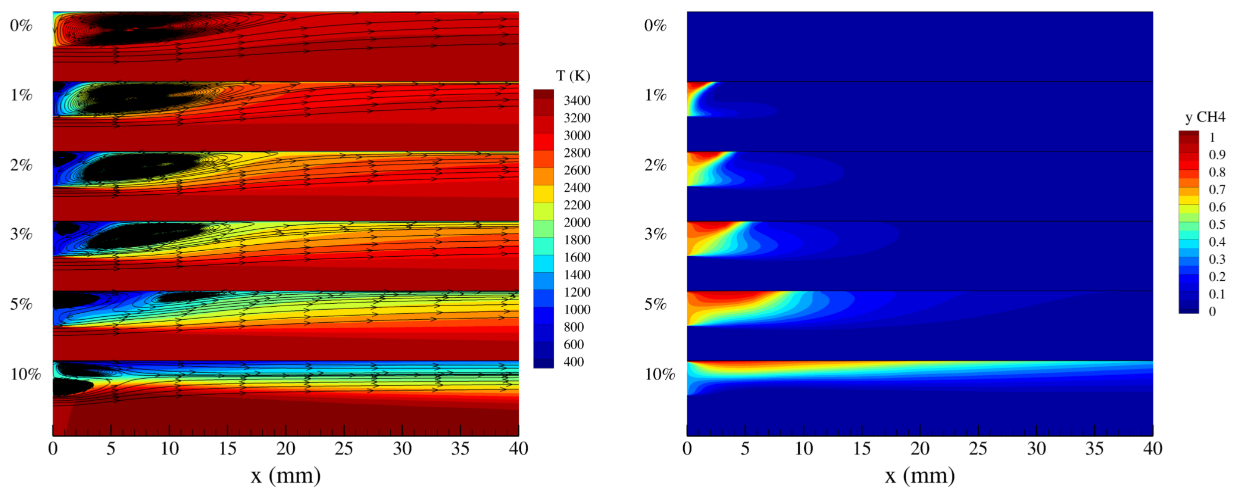

(a) Temperature field and streamlines.

(b) Methane mass fraction field.

Figure 7: Film mass flow rate effect on flowfield at constant total mixture ratio for Tests 2-6.

From Table 5 it can be noticed that the specific impulse increases for low film mass flow rates. This behaviour is due to the fact that by keeping the overall mixture ratio constant (O/F_{tot} = 2.65), as the film mass flow rate increases, the injector mixture ratio O/F_{inj} corresponds to slightly higher temperatures and characteristic velocities (see Fig. 8).

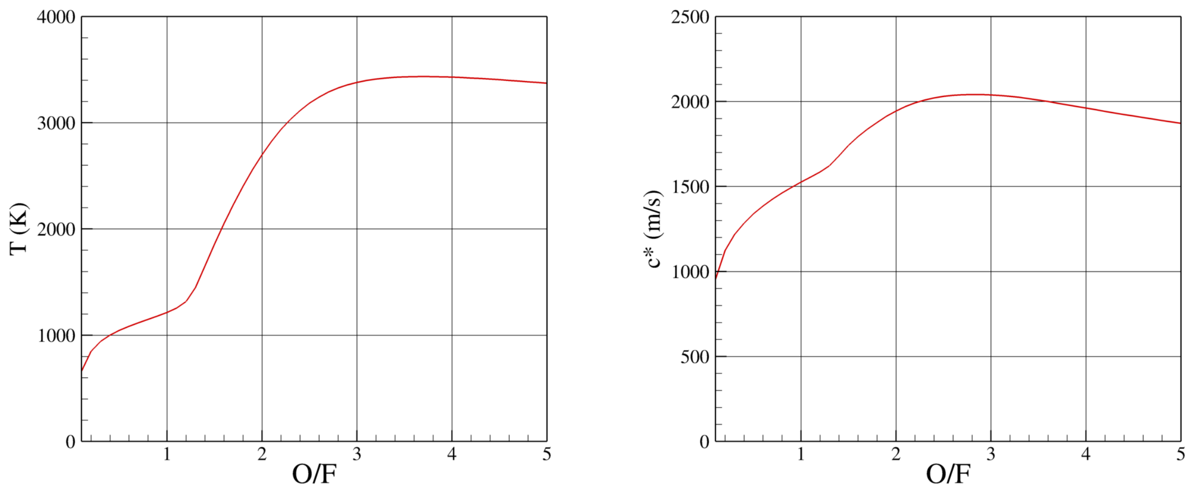

(a) Total temperature

(b) Characteristic velocity

Figure 8: Mixture ratio effect on CEA output.

DOI: 10.13009/EUCASS2023-657

For this reason, tests 7.1, 8.1 and 9.1 are performed with a constant injector mixture ratio equal to the reference one (O/F_{inj} = 2.65 for Test 1). This leads to a fixed temperature core flow which can aid the comparative analysis of the film cooling effect. In this approach, the fuel and oxidizer mass flow rates are not preserved separately, which alters the global mixture ratio towards fuel-rich conditions as the film mass flow rate is increased. The total mass flow rate is instead kept the same. The effect of this new strategy on the wall heat flux is shown in Fig. 9.

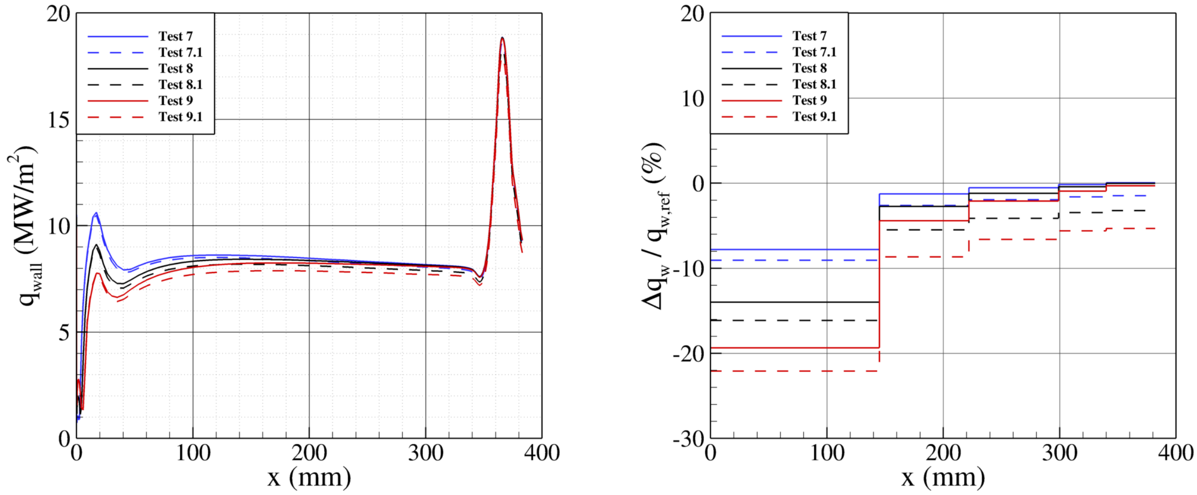

(a) Convective wall heat flux.

(b) Averaged convective wall heat flux.

Figure 9: Film mass flow rate effect on convective heat transfer at constant injector mixture ratio for Tests 7.1, 8.1 and 9.1.

From Fig. 9 the two different approaches can be observed and compared, the solid lines representing the constant total O/F_{tot} cases while the dashed lines the constant injection O/F_{inj} ones. The convective wall heat flux reduction is attenuated in the case of constant O/F_{tot}, compared to the O/F_{inj} one, due to the presence of a higher temperature core flow. In future work, it would be more appropriate to also consider different values of the overall mixture ratios.

4.4 Convective wall heat flux and performance reduction numerical correlations

From the previous numerical results, it is clear that the main driving parameter is represented by the film mass flow rate ratio ($\dot{m}_{film}/\dot{m}_{tot}$). It is reasonable to expect a direct link between heat flux and performance variation with this specific parameter. The convective wall heat flux reduction in both cylindrical and nozzle regions and vacuum specific impulse loss are well described by the correlation laws shown in Eqs. (10), (11), and (12). The correlation laws are also represented as dashed lines in Fig. 10.

$$\left.\frac{\Delta q_w}{q_{w,ref}}\right|_{cyl} = -a_1 \left(\frac{\dot{m}_{film}}{\dot{m}_{tot}}\right) \tag{10}$$

$$\left.\frac{\Delta q_w}{q_{w,ref}}\right|_{noz} = -b_1 \left(\frac{\dot{m}_{film}}{\dot{m}_{tot}}\right)^{b_2} \tag{11}$$

$$\frac{\Delta I_{sp}}{I_{sp,ref}} = -c_1 \left(\frac{\dot{m}_{film}}{\dot{m}_{tot}}\right)^{c_2} \tag{12}$$

As it can be seen from Eq. (10), a linear relationship is expected between the combustion chamber convective wall heat flux reduction and the mass flow rate ratio. The coefficient a_1 is equal to 2.387 for the constant overall mixture ratio cases and 3.710 for the constant injector mixture ratio ones. The lowest slope is related to the fact that combustion products are characterized by a higher temperature in the case of constant overall mixture ratio leading to a reduced survival of the protective cold film layer.

DOI: 10.13009/EUCASS2023-657

A power law, Eq. (11), with a multiplicative factor b_1 of 0.002223 and 1.426 and a film mass flow rate ratio exponent b_2 of approximately 2.6 and 1 is found to provide the best interpolation, respectively, for nozzle wall heat flux reduction in the constant overall mixture ratio configurations and constant injector ones.
On the other hand, a simple power law is not able to fit the obtained specific impulse variation for the constant total O/F cases due to the non-monotonic trend. In the case of constant injector O/F, the coefficients c_1 and c_2 are equal to 0.15 and 1.479.

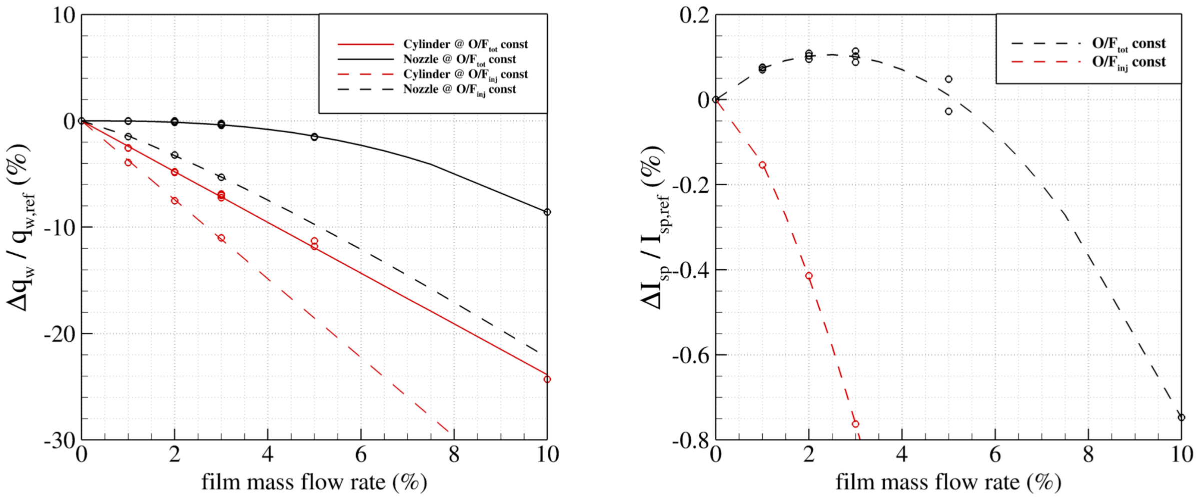

(a) Cylinder and nozzle convective wall heat flux fitting

(b) Specific impulse fitting

Figure 10: Correlation laws and numerical data.

The fitting procedure showed a goodness of fit between 99 and 100%. It is worth to recall that the found regression laws are valid for the investigated range of film mass flow rate ratios from 0 to 10% for constant overall mixture ratio and from 0 to 3% for the constant injector mixture ratio configuration. The presence of slightly scattered numerical data is due to the second-order effect induced by the film cooling injection slot height.

4.5 Chemical reaction mechanisms comparison

The presence of a secondary flow composed of pure gaseous methane yields a great variation of the mixture ratio passing from the boundary layer towards the core flow. Therefore the flowfields are characterized by different fluid dynamic and chemical conditions which have to be correctly taken into account by the selected chemical mechanisms. Here the JLR (global reaction mechanism) and TSR-CDF-13 (skeletal reaction mechanism) are compared in terms of convective wall heat flux and specific impulse evaluations (Figs. 11 and 12).

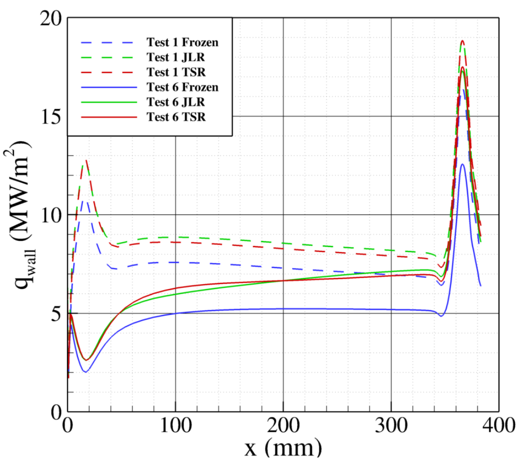

Figure 11: Chemical reaction mechanism effect on convective wall heat flux for Tests 1 and 6.

DOI: 10.13009/EUCASS2023-657

As evident from Figs. 11 and 12, chemical kinetics plays an essential role in the convective wall heat flux and performance evaluation. From the comparison between frozen and reactive simulations, it is clear that the presence of exothermic wall recombination reactions and the evolution of the flow chemical composition during the process of fluid dynamic expansion in the nozzle produces an increase in convective wall heat flux and performance in terms of specific impulse.

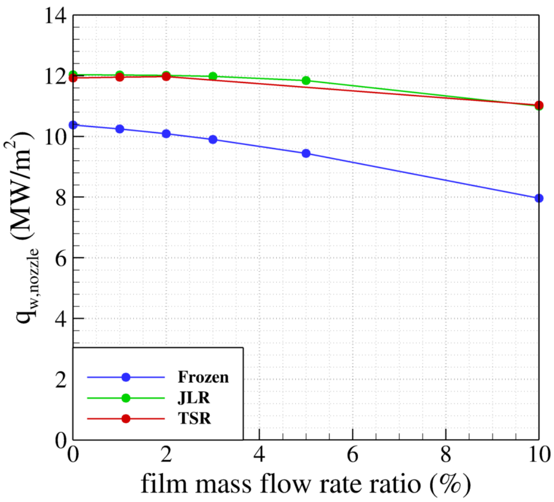

(a) Nozzle convective wall heat flux.

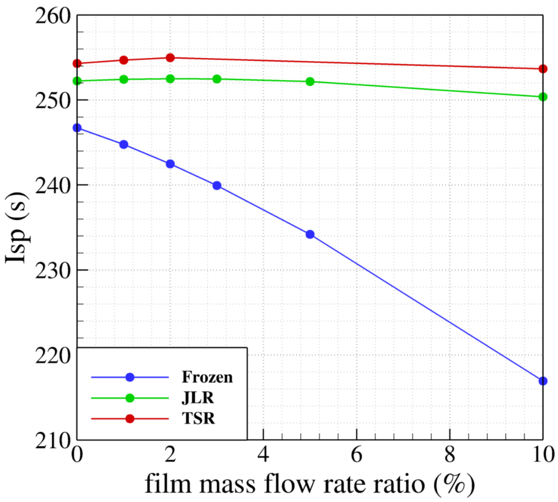

(b) Specific impulse.

Figure 12: Chemical reaction mechanism comparison.

Concerning the comparison between JLR and TSR-CDF-13 reactive simulations similar nozzle wall heat flux (Fig. 12a), temperature and methane mass fraction flowfields (Fig. 13a and 13b) are obtained. Differences in thrust chamber performance can be observed in Fig. 12b, in particular, the skeletal mechanism presents a higher specific impulse due to the slightly higher temperature achieved during the expansion process (Fig. 13c). The JLR global reaction mechanism is able to reliably represent the flow physics at a reduced computational cost, which makes it a useful tool during the design of LRE thrust chambers.

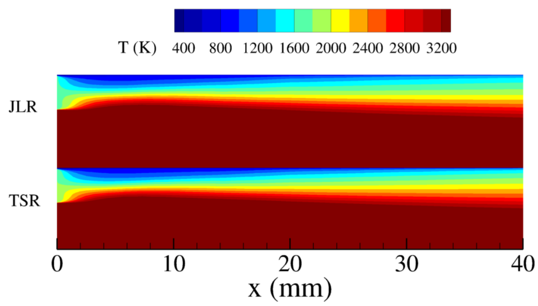

(a) Temperature field.

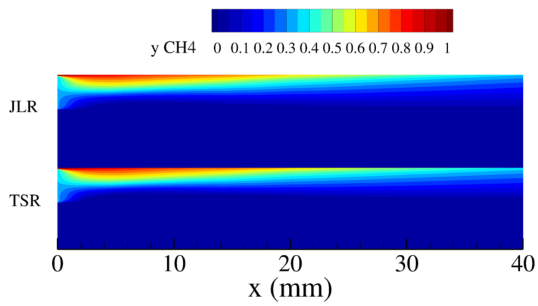

(b) Methane mass fraction field.

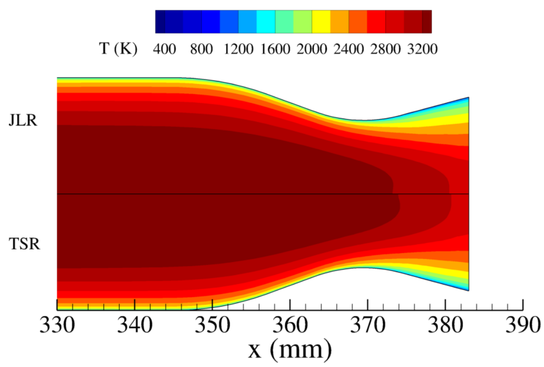

(c) Temperature field. Zoom in the nozzle region.

Figure 13: Chemical reaction mechanism flowfield comparison.

DOI: 10.13009/EUCASS2023-657

5. Preliminary Analysis of Mixture Ratio Bias

Numerical simulations featuring mixture ratio bias do not foresee a secondary flow injection in the immediate vicinity of the wall, as a bias in mixture ratio usually occurs at the outer injector row. Such a geometry is schematically shown in Fig. 1c. Two different local mixture ratios can be identified in such a configuration, one for the hot gas injection O/F_{inj}, and one for the peripheral flow O/F_{bias}. In order to evaluate the chemical composition and total temperature, a full mixing and combustion is assumed also at the outer row of injectors. The peripheral mixture ratio and bias mass flow rate are the investigated parameters in this case, therefore the values of the near-injector geometric quantities are fixed. An injection slot height of 100 μm placed in the middle of the backward facing step is hereafter considered.
The preliminary simulations for mixture ratio bias analysis are summarized in Table 6. The total mass flow rate and total mixture ratio of Table 4, a uniform wall temperature of 400 K, and the JLR global reaction mechanism are taken into account. Test 1 is also in this case the reference solution.

Table 6: Summary of mixture ratio bias parametric analysis obtained varying bias mass flow rate ratio and bias mixture ratio.

TEST	$\frac{\dot{m}_{bias}}{\dot{m}_{tot}}$	B	O/F_{tot}	O/F_{inj}	O/F_{bias}	$\frac{\Delta q_w}{q_{w,ref}}\Big\vert_{cyl}$	$\frac{\Delta q_w}{q_{w,ref}}\Big\vert_{noz}$	$\frac{\Delta I_{sp}}{I_{sp,ref}}(\%)$
14	0.02	1.088	2.650	2.685	1.500	-0.0131	0.0030	0.060
15	0.02	1.088	2.650	2.666	2.000	-0.0090	0.0039	0.058
16	0.03	1.649	2.650	2.701	1.500	-0.0217	0.0046	0.098
17	0.03	1.649	2.650	2.675	2.000	-0.0156	0.0057	0.095

In Figs.14a and 14b the effect of the bias mass flow rate and peripheral mixture ratio on the averaged convective wall heat flux is shown. In order to compare mixture ratio bias with previous film cooling results, tests 3 and 4 are also reported and indicated with $O/F_{bias} = 0.0$.

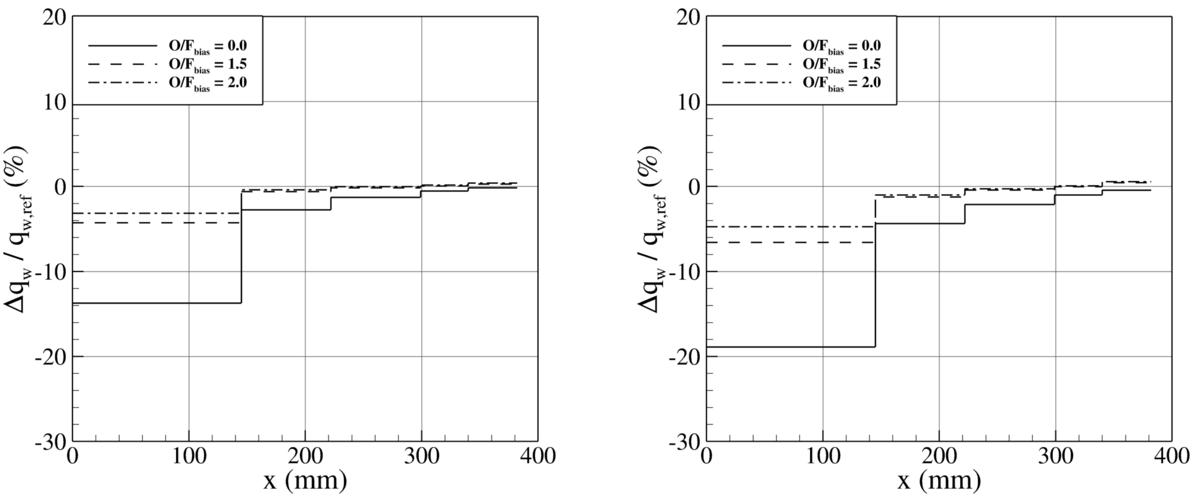

(a) $\dot{m}_{bias}/\dot{m}_{tot} = 2\%$

(b) $\dot{m}_{bias}/\dot{m}_{tot} = 3\%$

Figure 14: Bias mass flow rate and peripheral mixture ratio bias effect on averaged convective wall heat flux for Tests 14-17.

Bias mass flow rate cooling plays a similar role as the already seen film cooling strategy, with less impact on the wall heat flux reduction. An increase in the peripheral mass flow rate results in a convective wall heat flux decrease. The lower bias mixture ratio with respect to the nominal one is characterized by a different chemical composition and injection temperature of the peripheral flow (see Fig. 8a) resulting in cooler fluid layer close to the wall as $O/F_{bias} \to 0$ moves towards a pure methane injection. Mixture ratio bias cooling strategy can be envisioned in cases where a reduced wall heat flux decrease, as well as a reduced impact on the specific impulse, is needed.

DOI: 10.13009/EUCASS2023-657

6. Conclusions

This study aimed at performing numerical simulations of film-cooled and mixture-ratio-biased LRE thrust chamber burning gaseous oxygen and gaseous methane.
In case of the film cooling technique, it has been shown that the film mass flow rate is the most relevant parameter to be taken into account, while the effects of film injection temperature and slot height are deemed of secondary importance. Two different strategies have been investigated, one with constant total mixture ratio, and the other with constant injector mixture ratio. The latter strategy has been introduced in order to better evaluate the performance loss in terms of specific impulse. A numerical correlation for the wall heat flux reduction in both cylindrical and nozzle regions, and for the performance loss, have been provided. The JLR global reaction mechanism, with a limited number of chemical species and reactions, has provided results similar enough to the ones obtained with a skeletal reaction mechanism. This allows for significant savings of computational time and can aid the reliable prediction of the convective wall heat flux of LRE thrust chambers.
Regarding the mixture ratio bias cooling technique, the bias mass flow rate and bias mixture ratio have shown a significant effect on heat transfer and performance reduction. While the bias mass flow rate plays a role which is quite similar to the one of film cooling, the bias mixture ratio represents an interesting parameter to act on to find the best trade-off between wall heat reduction and performance loss. A mixture ratio bias can be useful in such cases where a small support for the regenerative cooling system is required, with a small loss in terms of specific impulse.

References

[1] G. P. Sutton and O. Biblarz. *Rocket Propulsion Elements*. John Wiley & Sons, Inc., Hoboken, New Jersey, USA, 2010.

[2] R. Cook and R. Quentmeyer. Advanced cooling techniques for high-pressure, hydrocarbon-fueled rocket engines. In *16th Joint Propulsion Conference*, page 1266, 1980.

[3] R. Arnold, D. I. Suslov, and O. J. Haidn. Film cooling in a high-pressure subscale combustion chamber. *Journal of propulsion and power*, 26(3):428–438, 2010.

[4] E. Martelli, F. Nasuti, and M. Onofri. Numerical analysis of film cooling in advanced rocket nozzles. *AIAA journal*, 47(11):2558–2566, 2009.

[5] G. Leccese, D. Bianchi, B. Betti, D. Lentini, and F. Nasuti. Convective and radiative wall heat transfer in liquid rocket thrust chambers. *Journal of Propulsion and Power*, 34(2):318–326, 2018.

[6] S. Silvestri, M. P. Celano, G. Schlieben, and O. J. Haidn. Characterization of a multi-injector GOX/CH4 combustion chamber. AIAA Paper 2016–4992, July 2016.

[7] S. Silvestri, C. Kirchberger, G. Schlieben, M. P. Celano, and O. J. Haidn. Experimental and numerical investigation of a multi-injector GOX/CH4 combustion chamber. *Transactions of the Japan Society for Aeronautical and Space Sciences, Aerospace Technology Japan*, 16(5):374–381, 2018.

[8] N. Perakis, D. Rahn, O. J. Haidn, and D. Eiringhaus. Heat transfer and combustion simulation of seven-element o2/ch4 rocket combustor. *Journal of Propulsion and Power*, 35(6):1080–1097, 2019.

[9] M. Pizzarelli, F. Nasuti, R. Paciorri, and M. Onofri. Numerical analysis of three-dimensional flow of supercritical fluid in cooling channels. *AIAA Journal*, 47(11):2534–2543, 2009.

[10] B. Betti, E. Martelli, F. Nasuti, and M. Onofri. Numerical study of heat transfer in film cooled thrust chambers. AIAA Paper 2012-3907, 2012.

[11] B. Betti, D. Bianchi, F. Nasuti, and E. Martelli. Chemical reaction effects on heat loads of ch4/o2 and h2/o2 rockets. *AIAA Journal*, 54(5):1693–1703, 2016.

[12] Pierluigi Concio, Mario Tindaro Migliorino, Daniele Bianchi, and Francesco Nasuti. Numerical estimation of nozzle throat heat flux in oxygen-methane rocket engines. *Journal of Propulsion and Power*, pages 1–13, 2022.

[13] Pierluigi Concio, Mario Tindaro Migliorino, Daniele Bianchi, and Francesco Nasuti. Numerical analysis of film cooling and mixture ratio bias in oxygen-methane liquid rocket engines. In *AIAA SCITECH 2023 Forum*, page 0513, 2023.

DOI: 10.13009/EUCASS2023-657

[14] J. D. Anderson. *Hypersonic and High-Temperature Gas Dynamics*. AIAA Education series, Reston, VA, 2006.

[15] K. Sutton and P. Gnoffo. Multi-component diffusion with application to computational aerothermodynamics. AIAA Paper 98-2575, June 1998.

[16] J. O. Hirschfelder, C. F. Curtiss, and R. B. Bird. *Molecular Theory of Gases and Liquids*. John Wiley & Sons, Inc., New York, USA, 1954.

[17] B. J. McBride, M. J. Zehe, and S. Gordon. Nasa glenn coefficients for calculating thermodynamic properties of individual species. NASA/TP–2002–211556, 2002.

[18] B. J. McBride and S. Gordon. Computer program for calculation of complex chemical equilibrium compositions and applications. NASA RP-1311, 1994.

[19] P. R. Spalart and S. R. Allmaras. A one-equation turbulence model for aerodynamic flows. *La Recherche Aerospatiale*, 1:5–21, 1994.

[20] W. P. Jones and R. P. Lindstedt. Global reaction schemes for hydrocarbon combustion. *Combustion and Flame*, 73:233–249, 1988.

[21] Alessio Frassoldati, Alberto Cuoci, Tiziano Faravelli, ELISEO Ranzi, C Candusso, D Tolazzi, et al. Simplified kinetic schemes for oxy-fuel combustion. In *1st International conference on sustainable fossil fuels for future energy*, pages 6–10, 2009.

[22] J. Liberatori, R. Malpica Galassi, D. Bianchi, F Nasuti, M. Valorani, and P. P. Ciottoli. A family of skeletal reaction mechanisms for methane-oxygen combustion at high pressure. *Journal of Propulsion and Power*, 2022.

[23] V. P. Zhukov. Kinetic model of alkane oxidation at high pressure from methane to n-heptane. *Combustion Theory and Modelling*, 13(3):427–442, 2009.

[24] J. Troe. Theory of thermal unimolecular reactions in the fall-off range. i. strong collision rate constants. *Berichte der Bunsengesellschaft für physikalische Chemie*, 87(2):161–169, 1983.

[25] R. G. Gilbert, K. Luther, and J. Troe. Theory of thermal unimolecular reactions in the fall-off range. ii. weak collision rate constants. *Berichte der Bunsengesellschaft für physikalische Chemie*, 87(2):169–177, 1983.

[26] P. L. Roe. Approximate Riemann solvers, parameter vectors and difference schemes. *Journal of Computational Physics*, 43:357–372, 1981.

[27] G. Strang. On the construction and comparison of difference schemes. *SIAM Journal on Numerical Analysis*, 5:506–517, 1968.

[28] P. N. Brown, G. D. Byrne, and A. C. Hindmarsh. Vode: A variable-coefficient ODE solver. *SIAM Journal on Scientific and Statistical Computing*, 10:1038–1051, 1989.